Title: Mechanical confinement induces ferroptosis through mitochondrial dysfuction

Authors: Fang Zhou[1], Chenlu Kang[1], Jiayi Li[1], Ao Yang[2], Robert J. Ju[3,4], Yujie Sun[5], Ling Liang[2], Xiaoqing Hu[6,*], Samantha J. Stehbens[3,4,*], Congying Wu[1,7,*]

Affiliations:

[1]Institute of Systems Biomedicine, School of Basic Medical Sciences, Peking University Health Science Center, Beijing, 100191 China.

[2]Department of Biochemistry and Biophysics, School of Basic Medical Sciences, Peking University Health Science Center, Beijing, 100191, China.

[3]The University of Queensland, Institute for Molecular Bioscience, St Lucia Brisbane, Queensland, Australia.

[4]The University of Queensland, Australian Institute for Bioengineering and Nanotechnology, St Lucia Brisbane, Queensland, Australia.

[5]State Key Laboratory of Membrane Biology, Biomedical Pioneer Innovation Center (BIOPIC), School of Life Sciences, Peking University, Beijing, 100871, China.

[6]Department of Sports Medicine, Institute of Sports Medicine of Peking University, Beijing Key Laboratory of Sports Injuries, Peking University Third Hospital, Beijing, 100191, China.

[7]International Cancer Institute, Peking University, Beijing, 100191, China.

*Correspondence:

Xiaoqing Hu, huxiaoqingbd01@sina.com.

Samantha J. Stehbens, s.stehbens@uq.edu.au.

Congying Wu, congyingwu@hsc.pku.edu.cn.

Abstract

Mechanical confinement due to cell crowding or migration through limited space is a key physical stimulus under physiological and pathological conditions, which can act on the nucleus-the stiffest organelle-to tailor various cellular behaviors. However, whether this process is involved in cell death and the underlying mechanisms remain unknown. Here, we demonstrate that mechanical confinement induces ferroptosis which might be triggered by nucleus deformation. In confinement, cells undergo not only cPLA2 translocation to mitochondria but also Drp1 phase separation-dependent mitochondrial fragmentation, causing the excessive production of arachidonic acid (ARA) and mitochondrial ROS (mtROS), respectively. The coordinated action of ARA and mtROS leads to lipid peroxidation and subsequent ferroptosis upon confinement. We further reveal that human osteoarthritis (OA) tissue exhibit highly lipid ROS level and cPLA2 localization to mitochondria. Cumulatively, our findings unveil a pivotal role of Drp1 and cPLA2 in linking mechanical confinement with mitochondrial dysfunction and ferroptosis, which may shed new lights on patho-physiological relevance of mechanical confinement.

Introduction

Cell motility is harnessed by protozoa to evade biochemical and biophysical adversities[1, 2]. In multicellular organisms, cells are also exposed to a multitude of mechanical forces[3-5]. Recent studies have unveiled the switch of mesenchymal to amoeboid migration models when mammalian cells are compressed or squeezed through narrow channels[6, 7]. Nonetheless, the fate and pathophysiological consequences of confined immobile cells are understudied.

Unlike chemical ligands that rely on surface receptors or transmembrane trafficking to transduce, biophysical constraints are able to propagate through deformation[8, 9]. Distinct mechanical features of the cytoskeleton and cellular

organelles constitute a plethora of force rulers, which act in combination with mechano-sensitive proteins to fine-gauge cellular mechano-response[10, 11]. Although the central dogma highlights the nucleus as the center of gene replication and expression, its function in the biochemical signal relay is less revealed. However, as the stiffest organelle inside the cell, increasing evidence has suggested the determinant role of the nucleus in mechano-sensation[12, 13].

Nuclear rupture when cells migrate through extremely small holes has been documented to accumulate DNA damage and be linked to carcinogenic and inflammogenic status[14-16]. Immune cells can detect inflammatory signals exposed to cell surfaces or released through dirty cell deaths in the form of pyroptosis, necroptosis, and ferroptosis[17, 18]. The latter of which has been reported in osteoarthritis (OA), a disease intimately associated with mechanical overloading[19]. Here, we report mechanical confinement induces ferroptosis. We observe not only cPLA2 translocation to mitochondria but also enhanced Drp1 phase separation and subsequent mitochondrial fragmentation upon nuclear deformation. Excessive cPLA2-catalyzed arachidonic acid (ARA) generation production alongside mitochondrial ROS (mtROS) concertedly leads to lipid oxidation and cell death. Finally, we demonstrate this mechano-stress response in OA. In conclusion, our findings shed light on how the cellular physical microenvironment manifests cell fate and identify a new mechanism centered on Drp1 and cPLA2 that links ferroptosis to mechanical stimuli related to human diseases.

Results

1. Mechanical confinement triggers ferroptosis

To study how confinement affects cell morphology and survival, we modified published axial cell confinement devices[20, 21] and vertically sandwiched cells between weighed optical glass and the culture dish (Figure 1A). Without spacers, cells burst instantaneously after applying confinement

(Movie S1). However, with 3 μm microsphere spacers that prevent cell rupture while providing cell and nuclear confinement[6, 20], we observed slow and step-wise cell death, suggestive of a programmed process. After 3-4 hours of unchanged cell morphology, plasma membrane blebbing appeared and lasted for 30 min until the eventual cell lysis (Movie S2). By 6 hours under 3 μm confinement, 80% of the cells were dead, indicated by propidium iodide (PI) staining (Figure 1B-1C). To exclude that this cell death was caused by sheer force or hypoxia during confinement, we used 20 μm microsphere spacers where cells were not in contact with the confinement roof[20] but experienced similar sheer force or hypoxia condition. The 20 μm spacers did not induce cell death (Figure S1A), indicating that cells undergo programmed cell death in response to prolonged confinement.

Cell swelling with large plasma membrane bubbles is characteristic of pyroptosis[22, 23]. However, in confined cells, we failed to detect the cleavage of GSDMD or GSDME, the pore-forming effectors in pyroptosis (Figure S1B). Moreover, the pan-caspase inhibitor Z-VAD-FMK used to stall pyroptosis[24, 25] failed to block this process (Figure S1C). Necroptosis has been reported in rat nucleus pulposus cells under continuous hydrostatic pressure[26]. However, we did not detect changes in the phosphorylation of MLKL, which is a hallmark of necroptosis (Figure S1D). Moreover, NSA inhibition of necroptosis also failed to block confinement-induced cell death (Figure S1E). Interestingly, we observed time-dependent increase in total and lipid ROS, which occur in ferroptosis[27, 28], starting at 2 hours under 3 μm (Figure 1D-1G) but not 20 μm confinement (Figure S1F), as assayed by the fluorescent probes DHE and BODIPY-C11 respectively. Consistently, the RNA expression of the ferroptosis biomarkers, acyl-CoA synthetase long-chain family member 4 (ACSL4) and cyclooxygenase-2 (COX2) increased after confinement (Figure 1H). In addition, we found that a variety of ferroptosis inhibitors, including DFOM, ferrostatin-1 (Fer-1), liproxstatin-1 (Lip-1), and Trolox, remarkably diminished confinement induced-cell death (Figure 1I). These data suggest that the cell death induced

by confinement may be ferroptosis.

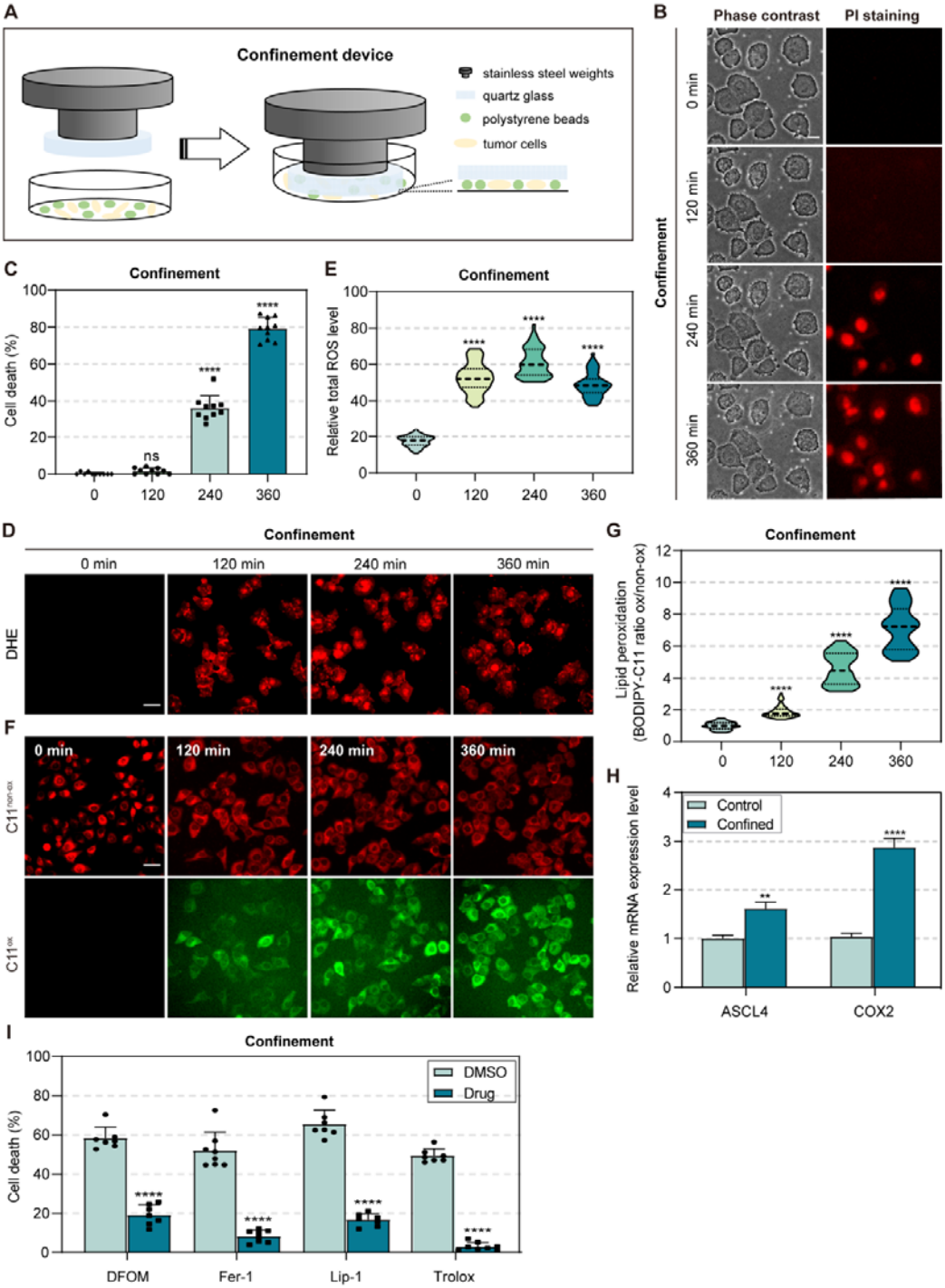

Figure 1. Mechanical confinement triggers ferroptosis. (A) Schematic diagram of the cell confinement device. Combining stainless steel weight, quartz glass, and polystyrene microspheres of different sizes, we can vertically restrict cell height by sandwiching cells between glass and culture dish. The polystyrene microspheres of defined diameters act as spacers to control the confinement height. (B) Representative time-lapse images showing the propidium iodide (PI) staining (red, 10 μM) of

HeLa cells during confinement. Scale bar = 20 μm. (C) Quantification of cell death ratio of HeLa cells during confinement. The cell death is measured by PI staining and cell death (%) = PI positive cells/total cells * 100. Data are shown as mean ± SD. (*N* = 10 fields, ns represents not significant, ****$p < 0.0001$, unpaired one-way ANOVA with Tukey's test). (D) Representative time-lapse images of dihydroethidium (DHE) staining (red, 10 μM for 1 hour) indicated total ROS level in HeLa cells during confinement. Scale bar = 40 μm. (E) Quantification of total ROS level in HeLa cells during confinement. Violin plot center lines denote the median, and dashed lines represent the 25th and 75th percentiles. (*N* = 50 cells, ns represents not significant, ****$p < 0.0001$, unpaired one-way ANOVA with Tukey's test). (F) Representative time-lapse images showing BODIPY-C11 581/591 staining (5 μM for 1 hour) indicated lipid ROS level in HeLa cells during confinement. Non-oxidative state (red), oxidative state (green). Scale bar = 40 μm. (G) Quantification of lipid ROS level in HeLa cells during confinement. Data was calculated by BODIPY-C11 fluorescence intensity ratio of oxidative/non-oxidative. (*N* = 50 cells, ****$p < 0.0001$, unpaired one-way ANOVA with Tukey's test). (H) qRT-PCR assay showing the ASCL4 and COX2 mRNA levels in HeLa cells upon confinement or not. Data are shown as mean ± SD. (**$p < 0.01$, ****$p < 0.0001$, unpaired two-way ANOVA with Sidak's test). (I) The cell death ratio in HeLa cells treated with DMSO or ferroptosis inhibitors upon confinement, including DFOM (100 μM), ferrostatin-1 (Fer-1, 1 μM), liproxstatin-1 (Lip-1, 0.5 μM), and Trolox (200 μM). Data are shown as mean ± SD. (*N* = 7 or 8 fields, ****$p < 0.0001$, unpaired two-way ANOVA with Sidak's test).

2. cPLA2 is activated and translocates to mitochondria upon confinement

Next, we sought to identify potential mechanosensory mechanisms that may contribute to ferroptosis in confinement. Using the Piezo inhibitor and siRNAs against integrins, we ruled out that these mechano-sensors played a determinant role during this process (Figure S2A-S2B). Aside from these mechano-sensors, the nucleus has recently been viewed as a mechano-gauge[12, 13]. It can actively convert mechanical input into signaling or transcriptional output through its dynamic changes in structure and morphology[29]. Consistent with previous studies, we found 35% increase in the nucleus projected surface area[12] under 3 μm but not 20 μm confinement (Figure 2A-2B), indicative of nuclear deformation.

Nuclear deformation can activate cytosolic phospholipase 2 (cPLA2) to produce ARA[12, 13], which can be metabolized to synthesize lipid hydroperoxides, which are the prerequisites for ferroptosis[30]. Thus, we asked

whether cPLA2 activation may trigger confinement-induced ferroptosis. When we depleted cells of cPLA2 (cPLA2 KD) (Figure S2C), we observed a reduction in lipid ROS level and largely abrogation of cell death in confined cells (Figure 2C-2E). Similar scenarios were reproduced with the cPLA2 inhibitor CAY10650 (Figure 2F-2G), arguing that the catalytic role of cPLA2 is critical for confinement-induced ferroptosis.

cPLA2 has been reported to translocate from the nucleoplasm to the nuclear envelope upon nuclear deformation[31]. However, live cell imaging of cPLA2-EGFP expressing cells under confinement did not show nuclear envelope translocation (Figure S2D). Interestingly, we observed cPLA2 translocation to mitochondria starting at 90 min under confinement (Figure 2H-2I, Movie S3), similar to the previous report of mitochondrial translocation and activation of cPLA2 following sphingolipid lactosylceramide treatment in astrocyte[32]. The confinement-induced mitochondria translocation of cPLA2 was not seen with 20 μm height (Figure S2E) or enucleated cytoplasts (Figure 2J, Figure S2F-S2G), indicating a critical role of nuclear deformation.

However, we treated cells with increasing concentrations of ARA and observed negligible impacts on lipid ROS level and cell viability (Figure 2K-2L). Collectively, these data suggest that cPLA2 activation responds to nuclear confinement but is insufficient to trigger ferroptosis.

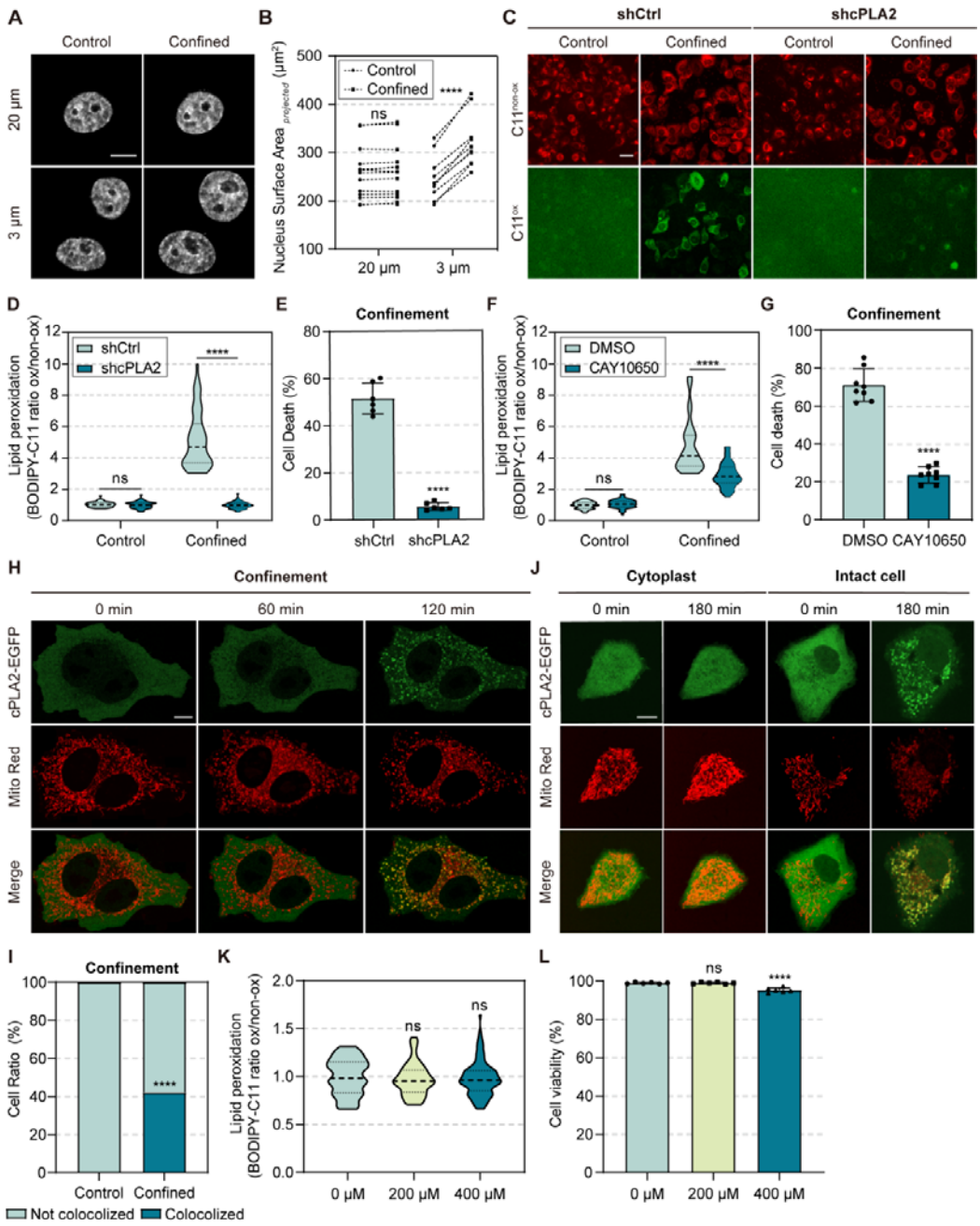

Figure 2. cPLA2 is activated and translocates to mitochondria upon confinement. (A) xy views of the Hoechst-stained nucleus before and after 20 µm (top) or 3 µm (bottom) confinement. Scale bar = 10 µm. (B) Quantification of projected nucleus surface area upon confinement. ($N_{20\ \mu m}$ = 14, $N_{3\mu m}$ = 10, ns represents not significant, ****p < 0.0001, statistical significance is determined via paired two-way ANOVA with Sidak's test). (C) Representative images of BODIPY-C11 581/591 staining in control (shCtrl) and cPLA2 knockdown (shcPLA2) HeLa cells upon confinement or not. Scale bar = 40 µm. (D) Quantification of lipid ROS level in shCtrl and shcPLA2 HeLa cells. (N = 50 cells, ns represents not significant, ****p < 0.0001, paired two-way ANOVA with Sidak's test). (E) Cell death ratio of shCtrl and shcPLA2 HeLa cells upon confinement. Data are shown as mean ± SD. (N = 6 fields, ****p < 0.0001,

unpaired Student's t test). (F) Lipid ROS level in HeLa cells treated with DMSO for control or CAY10650 (150 nM). (N_{DMSO} = 60 cells, $N_{CAY10650}$ = 66 cells, ns represents not significant, ****p < 0.0001, unpaired two-way ANOVA with Sidak's test). (G) Cell death ratio in HeLa cells treated with DMSO or CAY10650 upon confinement. Data are shown as mean ± SD. (N = 8 fields, ****p < 0.0001, unpaired Student's t test). (H) Representative time-lapse images of the cPLA2-EGFP over-expressing HeLa cells stained with 200 nM MitoTrackerTM Red CMXRos (Mito Red) for 30 min during confinement. Scale bar = 10 μm. (I) Quantification of cell ratios that cPLA2-EGFP co-localizes with mitochondria under confinement. (N = 66 cells, ****p < 0.0001, Fisher's exact test). (J) Representative images of the localization relationship between cPLA2-EGFP and mitochondria indicated by Mito Red in intact HeLa cells or enucleated cytoplasts upon confinement. Scale bar = 10 μm. (K) Lipid ROS level in HeLa cells treated with increasing concentrations of ARA (0 μM, 200 μM and 400 μM). Cells in the 0 μM group are treated with DMSO for control. (N = 55 cells, ns represents not significant, unpaired one-way ANOVA with Tukey's test). (L) Cell viability in HeLa cells treated with increasing concentrations of ARA. Cell viability (%) = (total cells-PI positive cells)/total cells * 100. Data are shown as mean ± SD. (N = 6 fields, ns represents not significant, ****p < 0.0001, unpaired one-way ANOVA with Tukey's test).

3. Nuclear confinement elevates mitochondrial fission and mtROS

While monitoring cPLA2 mitochondrial translocation, we noticed that a majority of cells (87%) displayed mitochondrial fission under 3 μm but not 20 μm confinement (Figure 3A-3B, Movie S4). To specifically address the role of nuclear deformation, we utilized atomic force microscopy (AFM) with a flat tipless cantilever to compress and deform single cells above the nucleus, while monitoring mitochondrial morphology by live cell imaging. Notably, we observed rapid mitochondrial fission when the cantilever pressed down the cell and deformed the nucleus (Figure 3C-3D). Next, we generated cytoplasts containing preserved mitochondrial networks (Figure S3A) by centrifugation-based enucleation[33, 34]. Strikingly, when confined with 3 μm spacers, the enucleated cytoplasts were resisted to mitochondrial fragmentation (Figure 3E). These observations suggest that nuclear deformation is required to induce mitochondrial fission, prior to cell death.

Confinement-induced mitochondrial fission echoes the smaller mitochondria seen in ferroptotic cells[27, 35] and diverse mitochondrial metabolic

abnormalities in ferroptosis[36, 37]. Mitochondrial fission is executed by the dynamin-like GTPase Drp1[38]. Perturbation of Drp1 function by knocking down Drp1 (Figure S3B) or overexpressing the dominant negative mutant mcherry-Drp1-K38A (Drp1-K38A OE)[39] inhibited mitochondrial fragmentation (Figure 3F-3I), suggesting that confinement induced mitochondrial fission is mediated through Drp1. Mitochondrial fission is preceded with a pre-constriction step conferred by the ER contacting specific mitochondrial sites[40]. The rough ER is structurally linked with the outer nuclear membrane, and that nucleus deformation detects mitochondrial fission under confinement, we thus investigated ER-mitochondria contacts under confinement. We used the contact FP system[41], and observed that the number of ER-mitochondria contacts remained unchanged even after mitochondrial fragmentation during confinement (Figure S3C-S3D).

Using tetramethylrhodamine methyl (TMRM), We have also detected mitochondrial membrane depolarization under confinement (Figure 4A-4B), without Parkin translocation to mitochondria (Figure S4A), a key step in mitophagy. As mitochondria defects are responsible for increased mtROS[42] which has been implicated in lipid peroxidation and ferroptosis onset[43], we next examined whether mtROS level increases along with mitochondrial fission under cell confinement. Indeed, using Mito-roGFP2, we observed a significant increase of mtROS (Figure 4C-4D) under confinement. When we scavenged mtROS (Figure S4B) using Mito tempo, a mitochondria-targeted superoxide dismutase mimetic, in confined cells, we found significantly reduced total ROS and lipid ROS, as well as decreased cell death (Figure 4E-4G). A similar effect was seen with the antioxidant EUK134 or NAC (Figure S4C-S4D), suggesting that mtROS is a key player in confinement-induced ferroptosis. In addition, Drp1 KD alleviated the upregulation of total and lipid ROS level, and inhibited subsequent cell death in confinement (Figure 4H-4J). Taken together, these results indicate that Drp1-dependent mitochondrial fragmentation and elevated mtROS may play critical roles in

confinement-induced ferroptosis.

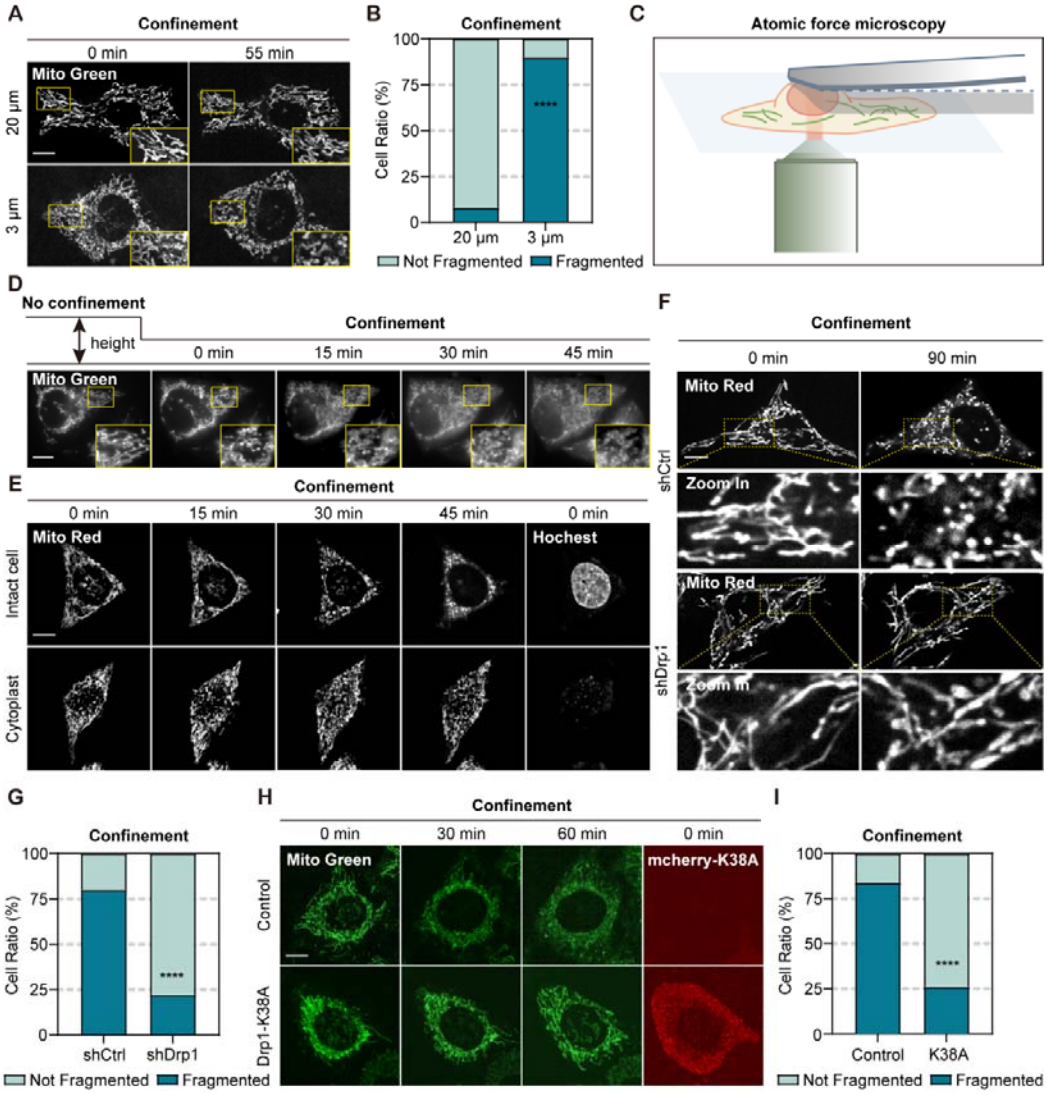

Figure 3. Nuclear confinement elevates mitochondrial fission. (A) Representative time-lapse images of mitochondria stained with 200 nM MitoTrackerTM Green FM (Mito Green) for 30 min in HeLa cells under 20 μm (top) or 3 μm (bottom) confinement. The yellow dashed boxes are zoomed in. Scale bar = 10 μm. (B) Quantification of cell ratios with fragmented mitochondria at 20 or 3 μm confinement for 60 min. (N = 50 cells, ****p < 0.0001, Fisher's exact test). (C) Schematic diagram of the experimental setup using atomic force microscopy (AFM) to compress single cell while microscopic imaging. (D) Representative time-lapse images of mitochondria stained with Mito Green in the HeLa cell compressed by AFM. The yellow dashed boxes are zoomed in. Scale bar = 10 μm. (E) Representative time-lapse of mitochondria stained with Mito Red in intact HeLa cells or enucleated cytoplasts during 45 min confinement. Nucleus were labeled by 5 μg/mL Hoechst for 20 min. Scale bar = 10 μm. (F) Representative images of mitochondria stained with Mito Red in control (shCtrl) and Drp1 knockdown

(shDrp1) HeLa cells after confinement for 0 or 90 min. The yellow dashed boxes are zoomed in. Scale bar = 10 μm. (G) Quantification of cell ratio with fragmented mitochondria in shCtrl and shDrp1 HeLa cells at confinement for 90 min. (N_{shCtrl} = 56 cells, N_{shDrp1} = 49 cells, ****p < 0.0001, Fisher's exact test). (H) Representative time-lapse image of mitochondria stained with Mito Green in HeLa cells expressing mcherry-Drp1-K38A during 60 min confinement. The control group is HeLa cells without transfection of mcherry-Drp1-K38A at the same culture dish. Scale bar = 10 μm. (I) Quantification of cell ratio with fragmented mitochondria in HeLa cells expressing mcherry-Drp1-K38A or in the control group at confinement for 60 min. (N = 50 cells, ****p < 0.0001, Fisher's exact test).

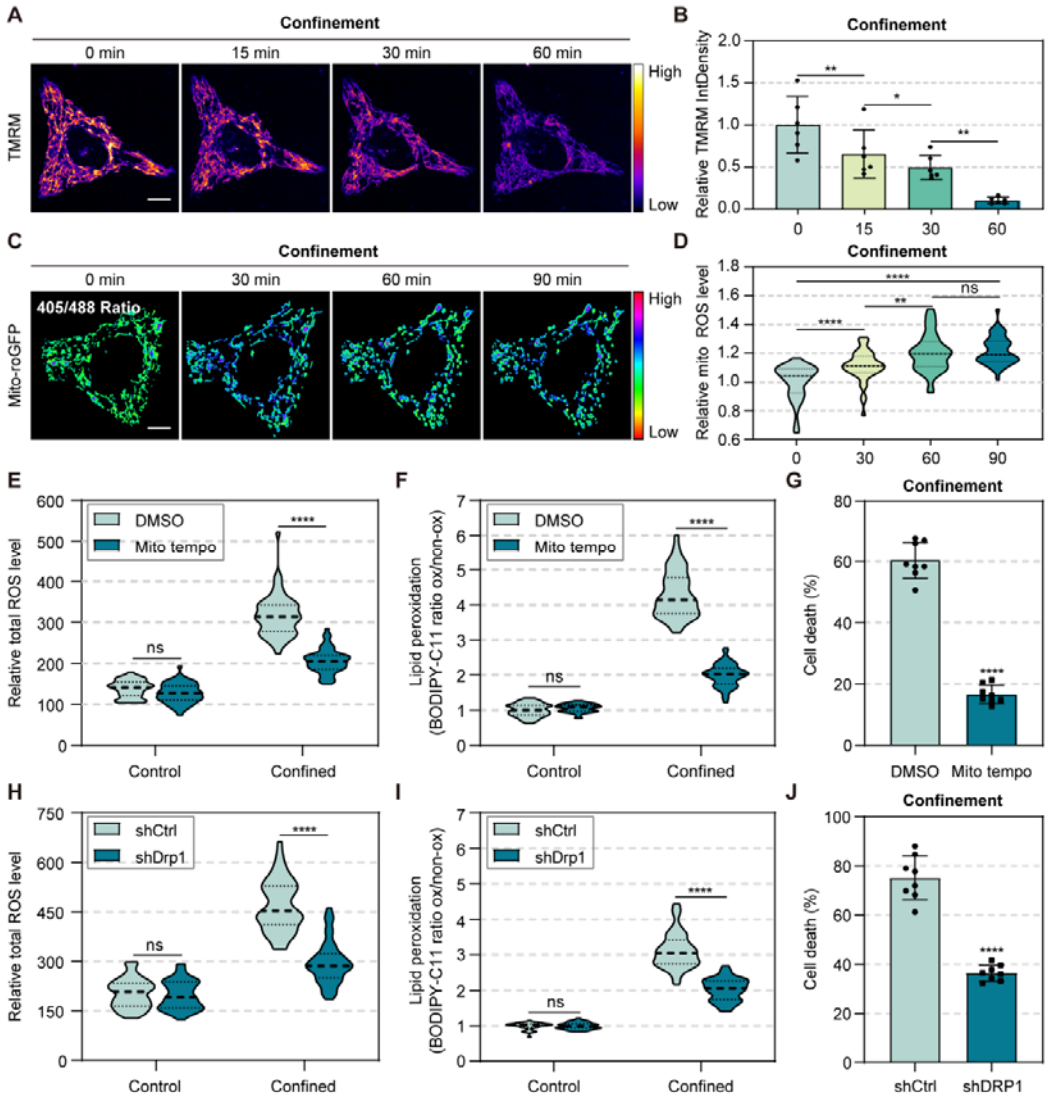

Figure 4. Nuclear confinement elevates mtROS to induce ferroptosis. (A) Representative time-lapse thermographs of TMRM staining (100 nM, 20 min) in HeLa cells during 60 min confinement. Scare bar = 10 μm. (B) Quantification of TMRM fluorescence intensity per cell under confinement, normalized by data at 0 min. Data are shown as mean ± SD. (N = 6 cells, ****P<0.0001, paired one-way ANOVA with

Tukey's test). (C) Representative time-lapse ratiometric images showing mtROS level in HeLa cells stably expressing Mito-roGFP during 90 min confinement. Scare bar = 10 μm. (D) Quantification of the relative mtROS level per cell in HeLa cells under confinement, normalized by data at 0 min. (*N* = 44 cells, ns represents not significant, ****p <0.0001, unpaired One-way ANOVA with Tukey's test). (E) Total ROS level detected by DHE staining in HeLa cells treated with DMSO or Mito tempo (10 μm) upon confinement or not. (*N* = 50 cells, ns represents not significant, ****p <0.0001, unpaired two-way ANOVA with Sidak's test). (F) Lipid ROS level in HeLa cells treated with DMSO or Mito tempo upon confinement or not. (*N* = 50 cells, ns represents not significant, ****p <0.0001, unpaired two-way ANOVA with Sidak's test). (G) Cell death ratio in HeLa cells treated with DMSO or Mito tempo upon confinement. Data are shown as mean ± SD. (*N* = 8 fields, ****p < 0.0001, unpaired Student's t test). (H) Total ROS level in shCtrl and shDrp1 HeLa cells upon confinement or not. (*N* = 50 cells, ns represents not significant, ****p <0.0001, unpaired two-way ANOVA with Sidak's test). (I) Lipid ROS level in shCtrl and shDrp1 HeLa cells upon confinement or not. (*N* = 40 cells, ns represents not significant, ****p <0.0001, unpaired two-way ANOVA with Sidak's test). (J) Cell death ratio in shCtrl and shDrp1 HeLa cells upon confinement. Data are shown as mean ± SD. (*N* = 8 cells, ****p < 0.0001, unpaired Student's t test).

4. Nuclear confinement increases cytoplasmic viscosity and Drp1-phase separation

To further elucidate the role of Drp1 in confinement-induced mitochondrial fragmentation, we generated a knockin cell line in which EGFP is fused to the N-terminus of Drp1 (Figure S5A) and monitored endogenous Drp1-EGFP signal in cells under confinement. Similar to the previous study[39], endogenous Drp1 was mainly diffusive in the cytoplasm, and some were present as puncta that co-localized with mitochondria (Figure S5B). Interestingly, the number of endogenous Drp1 puncta increased, and their co-localization with mitochondria enhanced (82.75% at 40 min vs. 74.42% at 0 min) in confined conditions (Figure 5A-5C). Moreover, the majority (90.79%) of mitochondrial fission sites we observed in confined cells showed Drp1 puncta localization (Figure 5D, Movie S5). The Drp1 puncta were reminiscent of droplet-like condensates formed during liquid-liquid phase separation (LLPS)[44]. We observed LLPS with purified Drp1 protein and detected liquid state as revealed from droplet fusion (Figure 5E-5F, Figure S5C-S5D). In addition, when we employed the optoDroplet system which is based on fusing protein of interest

with the light-sensitive oligomerization domain of Arabidopsis thaliana cryptochrome 2 (CRY2)[45], we found reversible formation of opto-Drp1 droplets upon blue light exposure in multiple cell lines (Figure 5G). While the GTPase domain was dispensable for its phase separation (Figure S5E), a series of disease-associated Drp1 point mutants[46] (A395D, R403C, C431Y) abrogated this property (Figure 5H, Figure S5F). Importantly, these LLPS mutants, when expressed in Drp1 KO cells (Figure S5G), resisted cell death induced by confinement (Figure 5I).

LLPS is regulated by protein concentration and crowding. It has been shown that confinement increases water efflux[47]. Therefore, we postulated that confinement may increase cytoplasmic viscosity and enhance molecular crowding. Using genetically encoded multimeric nanoparticles (GEMs), which are homomultimeric scaffolds fused to a fluorescent protein and can self-assemble into brightly stable tracer particles[48], we detected a time-dependent increase in cytoplasmic viscosity with confinement (Figure 5J).

The above evidence shows that the confinement can increase Drp1 phase separation and its co-localization with mitochondria, thereby enhancing mitochondrial fragmentation and subsequent ferroptosis. And the increased cytoplasmic viscosity may contribute to the enhanced Drp1 LLPS induced by confinement.

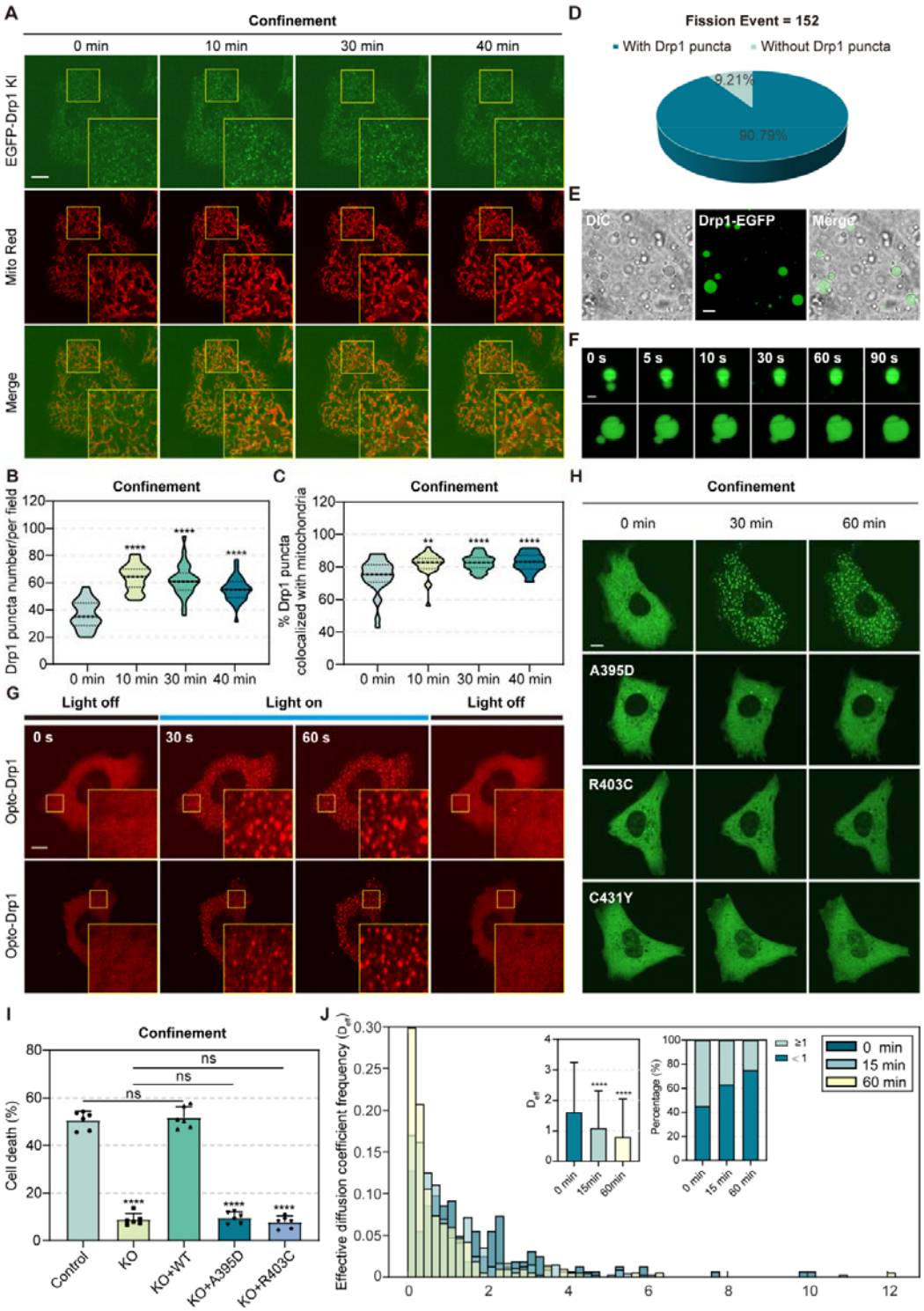

Figure 5. Nuclear confinement increases cytoplasmic viscosity and Drp1-phase separation. (A) Representative time-lapse images of endogenous EGFP-Drp1 KI HeLa cells stained with Mito Red during 40 min confinement. The yellow boxes are zoomed in. Scare bar = 10 μm. (B) Quantification of Drp1 puncta number per field at confinement for 0 min, 10 min, 30 min, and 40 min. (N = 30 fields from 18 cells, ****p < 0.0001, paired one-way ANOVA with Tukey's test). (C) Quantification of the proportion of

Drp1 puncta co-localized with mitochondria at confinement for 0 min, 10 min, 30 min, and 40 min. (N = 30 fields from 18 cells, **p < 0.05, ****p < 0.001, paired one-way ANOVA with Tukey's test). (D) Pie chart showing the proportion of fission sites with a Drp1 puncta. (N = 152 events from 7 cells). (E) Representative DIC and fluorescence images of purified Drp1-EGFP (20 μM) diluted in 200 mM NaCl containing 8% dextron. Scale bar = 10 μm. (F) Representative time-lapse images demonstrating small Drp1-EGFP droplets fusing into larger ones. Scale bar = 2 μm. (G) Representative images of HeLa cells expressing Opto-Drp1 when blue light is on/off. The yellow boxes are zoomed in. Scale bar = 10 μm. (H) Representative time-lapse images of HeLa cells over-expressing EGFP-tagged WT Drp1 or Drp1 variants (A395D, R403C, C431Y) during confinement. Scale bar = 10 μm. (I) Cell death ratio in Control, Drp1 KO, KO+WT (Drp1 KO rescued with wild-type EGFP-Drp1), KO+A395D (Drp1 KO rescued with EGFP-Drp1 A395D mutant) and KO+R403C (Drp1 KO rescued with EGFP-Drp1 R403C mutant) HeLa cells upon confinement. Data are shown as mean ± SD. (N = 6 fields, ns represents not significant, ****p < 0.0001, unpaired one-way ANOVA with Tukey's test). (J) Distribution of effective diffusion coefficients (D_{eff}) of 40 nm GEM particles within HeLa cells at confinement for 0 min, 15 min, and 60 min. Insets: (left) Bar chart showing D_{eff} within HeLa cells upon confinement. Data are shown as mean ± SD; (right) Quantification of the percentage of D_{eff} greater than 1 or less than 1 upon confinement. ($N_{0\ min}$ = 165 particles from 11 cells, $N_{15\ min}$ = 490 particles from 18 cells, $N_{60\ min}$ = 218 particles from 16 cells, ****p < 0.0001, unpaired one-way ANOVA with Tukey's test).

5. mtROS increase and cPLA2 activation concertedly trigger ferroptosis under nuclear confinement and in disease

Considering that mitochondrial fragmentation was observed prior to the mitochondrial translocation of cPLA2 (Figure 2H, Movie S3), we asked whether these two events were mechanistically linked. We monitored cPLA2 localization in Drp1 KD cells and found that cPLA2 can still translocate to mitochondria under confinement, albeit without mitochondria fragmentation (Figure 6A), suggesting that cPLA2 translocation to mitochondria might not be triggered by mitochondrial fragmentation. In addition, cPLA2 inhibition did not prevent mitochondrial fragmentation (Figure S6A-S6B) and total ROS generation (Figure S6C-S6D) induced by mechanical confinement. Generalizing lipid hydroperoxides from arachidonic acid requires cellular ROS[30]. We hypothesized that ARA could cooperate with ROS to induce ferroptosis. Indeed, when we added exogenous arachidonic acid and H_2O_2 to

cells, we observed potent cell death (Figure 6B-6C). Moreover, this synthetic lethality can be inhibited by Lip-1 and Fer-1 (Figure 6D).

Excessive mechanical loading of chondrocytes leads to ferroptosis, which may be closely associated with the pathogenesis of osteoarthritis (OA)[19]. We then asked whether ferroptosis and the above molecular events can be observed in the human OA tissues. We first detect the total ROS and lipid ROS levels in relative normal and OA regions in a human cartilage sample. We were able to observe higher total ROS (Figure 6E-6F) and lipid ROS (Figure 6G-6H) levels in OA regions. Next, we used a combination of cPLA2 and TOMM20 staining to observe the location of cPLA2. In chondrocytes of OA tissue, we found the partial co-localization of cPLA2 and TOM20 (Figure 6I-6K), indicating the localization of cPLA2 on mitochondria. These observations show that ferroptosis and cPLA2 translocation to mitochondria could also occur in vivo.

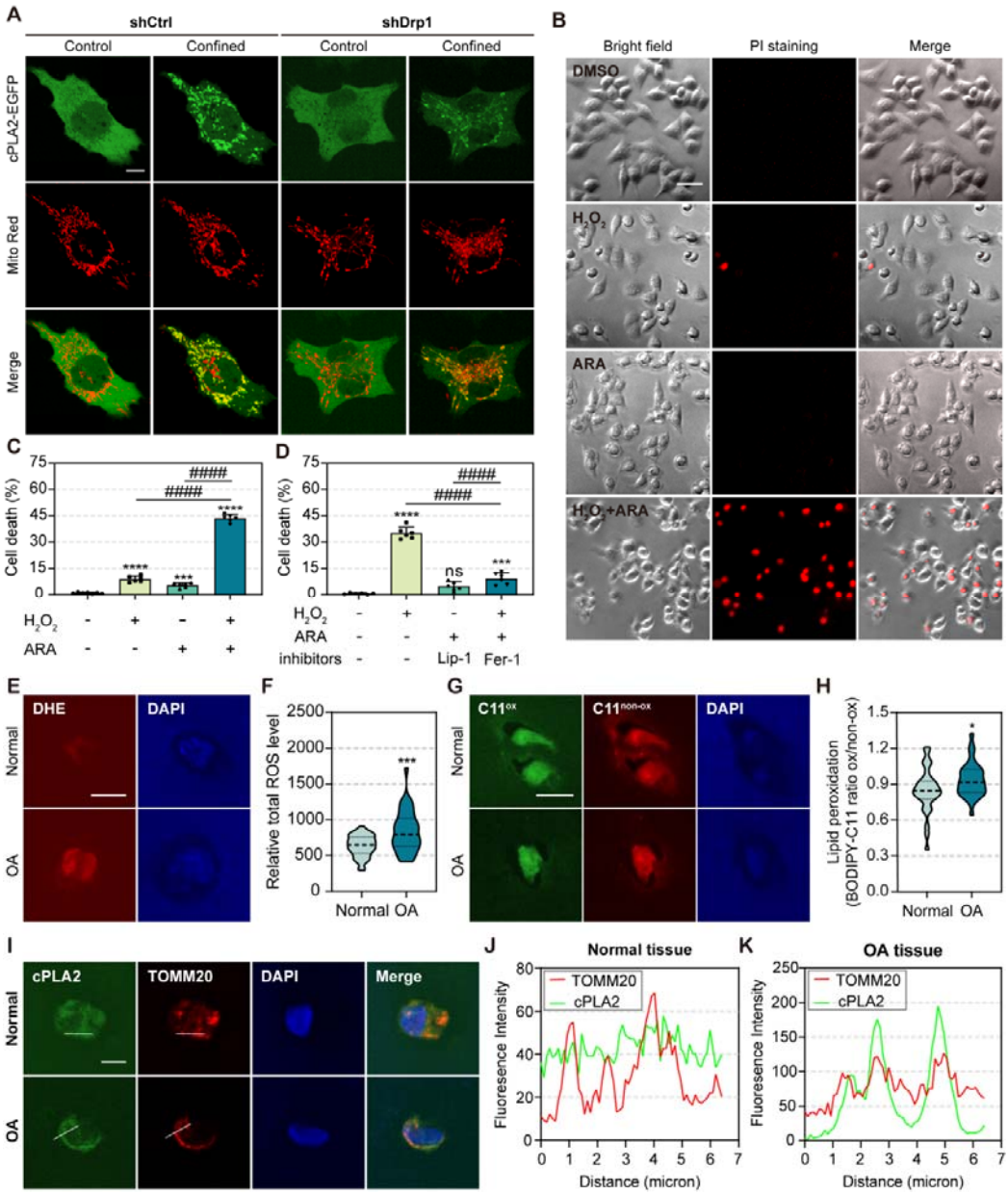

Figure 6. mtROS increase and cPLA2 activation concertedly trigger ferroptosis under nuclear confinement and in disease. (A) Representative images of the cPLA2-EGFP over-expressing shCtrl or shDrp1 HeLa cells stained with Mito Red upon confinement or not. Scale bar = 10 μm. (B) Representative bright field and fluorescence images of PI staining in HeLa cells treated with DMSO, H_2O_2 (400 μM) alone, ARA (400 μM) alone, and H_2O_2 + ARA. Scale bar = 40 μm. (C) Quantification of cell death ratio in HeLa cells related to B. Data are shown as mean ± SD. (N = 6 fields, $^{****}p < 0.0001$, $^{\#\#\#\#}p < 0.0001$, unpaired one-way ANOVA with Tukey's test). (D) Cell death ratio in HeLa cells treated with DMSO, H_2O_2 (400 μM) + ARA (400 μM), H_2O_2 + ARA + Lip-1 (10 μM), and H_2O_2 + ARA + Fer-1 (10 μM). Data are shown as mean ± SD. (N = 6 fields, ns represents not significant, $^{***}p < 0.001$, $^{****}p < 0.0001$, $^{\#\#\#\#}p < 0.0001$, unpaired one-way ANOVA with Tukey's test). (E) Representative images of DHE staining

(50 μM for 2 hours) in normal and OA tissues. The normal tissue and OA tissue are from the same sample. Total ROS (DHE, red), Nucleus (DAPI, blue). Scale bar = 10 μm. (F) Quantification of total ROS level in normal and OA tissue related to E. (N_{Normal} = 36 cells, N_{OA} = 34 cells, ****p < 0.0001, unpaired Student's t test). (G) Representative images of BODIPY-C11 581/591 staining (40 μM for 2 hours) in normal and OA tissues. Non-oxidative state (red), Oxidative state (green), Nucleus (DAPI, blue). Scale bar = 10 μm. (H) Quantification of lipid ROS level in normal and OA tissue related to G. (N = 30 cells, *p < 0.05, unpaired Student's t test). (I) Representative images of cPLA2 and TOMM20 in normal and OA tissue. cPLA2 (green), TOMM20 (red), Nucleus (DAPI, blue). Scale bar = 5 μm. (J-K). Line scan plot showing the distribution of cPLA2 and TOMM20 along the direction of the white arrowheads related to I in normal (J) and OA tissue (K).

Discussion

Cell behaviors responding to confined environments regulate cell fate and contribute to various physiological and pathological processes[6, 15, 49, 50]. Our research provides evidence that cells undergo ferroptosis driven by cPLA2 activation and disrupted mitochondrial homeostasis under confinement, which may exacerbate the progression of OA. Mitochondria form a highly dynamic tubular network within cells in normal conditions, while exhibiting fragmentation under confinement, indicating an imbalance between fusion and fission events. Mitochondrial fission involves initial membrane constriction followed by membrane scission. The former occurs almost at the ER-Mitochondria contact sites[40], where the ER tubule wraps around and constricts mitochondria by locally polymerizing actin to impose mechanical force[51]. We thus utilized contact-FP targeted to mitochondria and ER to visualize ER-mitochondria contacts and observe their dynamics under confinement. Nevertheless, the number of these contacts exhibits minor changes after confinement. There are two possibilities: One is that although ER-mitochondria contacts are stable structures, the membrane contacts between mitochondria and other organelles indeed increased, causing enhanced pre-constriction of mitochondria and subsequent recruitment of division machinery. For instance, the interaction between mitochondria and lysosomes also prompts

mitochondrial fission[52]. The other is that the heightened fission events under confinement may occur at pre-existing ER-mitochondria contacts. Altered biochemical processes at the ER-mitochondria contact interface under confinement, such as calcium transfer between these two organelles[53], regulate mitochondrial fission.

The master executor of mitochondria membrane scission has been coined to be Drp1[39]. It has been shown that Drp1 is recruited to the mitochondria outer membrane by adaptor proteins such as MFF, MID49/51, and then self-assembles into helix, wrapping the constriction sites[38]. Yet, it is still unclear how these proteins are regulated and how their activities are coordinated biochemically and biophysically to drive mitochondrial fission. Our study reveals that Drp1 is capable of undergoing phase separation. The dynamic endogenous Drp1 droplets are associated with mitochondria and this association increased under confinement. In addition, when utilizing optoDroplet system to induce Drp1 foci formation, the co-expressed cytoplasmic MFF or MID49/51 tagged with EGFP also condensates into droplets that co-localized with Drp1 (data not show). These results indicate that Drp1 and its adaptor proteins may assemble into division machinery at the mitochondria outer membrane through phase separation. However, it requires further study to confirm the involvement of Drp1 phase separation in mitochondrial fission and investigate the underlying mechanism in various conditions. The confinement-induced Drp1 phase separation may be triggered by the enhanced cytoplasmic molecular crowding since we observe a significant increase of the cytoplasmic viscosity, which may enhance the phase separation of proteins[48].

Our work shows that the nucleus may act as the mechanosensor in confinement-induced mitochondrial fission and subsequent ferroptosis since the enucleated cytoplasts exhibit resistance to mitochondria fragmentation and cPLA2 translocation to mitochondria caused by confinement. An emerging question is how nuclear deformation leads to mitochondrial fragmentation. The

nucleus has two enveloping membranes: the inner nuclear membrane (INM) and the outer nuclear membrane (ONM). The latter is continuous with ER and maintains well-established contacts[54]. While the ONM and ER are associated with stable ER-mitochondrial contacts, the membrane-associated structures connecting mitochondria and the nucleus have not been described. Thus, one potential mechanism for nucleus to regulate mitochondrial fission may involve the control of the morphology and function of ER. Although changes in nuclear shapes often directly modulate gene expressions in cells[55], and over 95% of mitochondrial proteins are encoded by nuclear DNA[56], the nucleus may not regulate mitochondrial fragmentation in confinement at the transcriptional or translational levels. Because mitochondrial fragmentation occurs early during confinement, starting from 30 to 60 min. Thus, further research on the relationship between nuclear deformation and mitochondrial fission will help elucidate the underlying interaction between the nucleus and mitochondria, shedding light on the ruler roles of nucleus in regulating cell biological processes under confinement.

Aberrant mechanical stimuli usually lead to traumatic events in cells and are linked to several diseases like cancer and OA[19, 57]. Our data implicate that nuclear deformation-mediated mitochondrial dysfunction coordinates cPLA2 to trigger ferroptosis under mechanical confinement, which may be involved in OA progression. This finding may provide a critical framework for further comprehensive understanding and targeting ferroptosis in treating OA and other diseases related to mechanical stresses.

Method

1.1 Cell culture

Human cervical carcinoma HeLa cells were a generous gift from Dr. Yong Liu (Xuzhou Medical University). Human embryonic kidney 293T (HEK293T) cells were a generous gift from Dr. Yuxin Yin (Peking University). Cells were cultured in Dulbecco's modified Eagle medium (DMEM; Corning, 10-013-CRVC) supplemented with 10% fetal bovine serum (FBS; PAN-Biotech, P30-3302), 100 U/mL penicillin and 100 μg/mL streptomycin (Macgene, CC004) at 37□ with 5% CO_2. For passage, the cells were washed with PBS (Macgene, CC010) and digested with trypsin-EDTA (Macgene, CC012). For long-term live cell imaging, cells were plated on the fibronectin (Sigma-Aldrich, F1056-5MG, 10 μg/mL)-coated 35 mm glass-bottom dishes (Cellvis, D35-10-1-N) and maintained in CO2-independent DMEM (Gibco, 18045-088) supplemented with 10% FBS, 100 U/mL penicillin and 100 mg/mL streptomycin at 37□ throughout the imaging process.

1.2 Plasmids construction and DNA transfection

The full-length human Drp1 was cloned using plasmid containing Drp1 from Dr. Yuhui Zhang (Huazhong University of Science and Technology) and subcloned into a lentiviral vector (Plvx-AcGFP-N1) with N-terminal tagged EGFP using an ABclonal MultiF Seamless Assembly kit (ABclonal, RK21020). The Drp1 truncations and single-point mutations were amplified and cloned into the same vectors. The FL-Drp1 (1-699 aa), GTPase domain (1-302 aa), ΔGTPase domain (303-699 aa), FL-Drp1-A395D, FL-Drp1-R403C and FL-Drp1-C431Y were constructed. The FL-Drp1-K38A was cloned from plasmid pcDNA-Drp1K38A (Addgene, #45161) and subcloned into Plvx-AcGFP-N1 with N-terminal tagged mCherry. Plasmid containing Cry2 was purchased from Addgene (#60032) to generate the Opto-droplet Optogenetic system (Opto-Drp1). The human cPLA2 was cloned from the HeLa cell-extracted

cDNA library and subcloned into Plvx-AcGFP-N1 with C-terminal tagged EGFP. The Contact-FP constructs (GA and GB) were cloned from GA-NES (Addgene, #61018) and GB-NES (Addgene, #61017), and were subcloned into the Plvx-AcGFP-N1 with C-terminal tagged full-length sequence of Sec61β (Plvx-GA-Sec61β) or mitochondrial localization sequence of MAVS (Plvx-GB-MAVS), respectively. The 40 nm GEM-Sapphire was cloned from pCDNA3.1-pCMV-PfV-GS-Sapphire (Addgene, #116933) and subcloned into Plvx-AcGFP-N1 backbone (Plvx-40 nm GEM).

For transient transfection, HeLa cells seeded on 6-well plates were transfected with 2 μg plasmid in opti-MEM (Invitrogen, 31985-070) containing 2 μL Neofect™ DNA transfection reagent (TF20121201) following the protocol for 24-48 h. For virus particle generation, HEK293T cells seeded on 10 cm culture dishes (Nest, 704201) were co-transfected with 5 μg interested plasmids, 3.75 μg packaging plasmids psPAX2, and 1.25 μg pCMV-VSV-G in opti-MEM containing 10 μL Neofect™ DNA transfection reagent.

1.3 Antibody and Reagents

The following antibodies were used in this study: rabbit anti-Drp1 (EPR19274, dilution 1:1000 for western blotting), rabbit anti-cleaved N-terminal GSDMD (EPR20829-408, dilution 1:1000 for western blotting), rabbit anti-GSDME (EPR19859, dilution 1:1000 for western blotting), rabbit anti-MLKL (EPR9514, dilution 1:1000 for western blotting), rabbit anti-GAPDH (EPR16891, dilution 1:4000 for western blotting) and mouse anti-β-actin (ab8226, dilution 1:2000 for western blotting) were purchased from Abcam; Rabbit anti-Drp1 (A21968, dilution 1:1000 for western blotting), rabbit anti-full-length GSDMD (A17308, dilution 1:1000 for western blotting), rabbit anti-cPLA2 (A0394, dilution 1:1000 for western blotting), rabbit anti-TOM20 (A19403, dilution 1:200 for immunofluorescence staining) and mouse anti-α-tubulin (AC012, dilution 1:3000 for western blotting) were purchased from Abclonal; Mouse anti-cPLA2(sc-454, dilution 1:100 for immunofluorescence staining),

anti-mouse (sc-516102, dilution 1:4000) and anti-rabbit (sc-2004, dilution 1:2000) horseradish peroxidase (HRP)-conjugated secondary antibodies were purchased from Santa Cruz Biotechnology. Anti-mouse Alexa Fluor 488 and anti-rabbit Alexa Fluor 555-conjugated secondary antibody were purchased from ThermoFisher Scientific.

For commercial reagents, Z-VAD-FMK (S7023), DFOM (S5742), Liproxstatin-1 (S7699), Ferrostatin-1 (S7243), and Mito-tempo (S9733) were purchased from Selleck. Trolox (ab120747) was purchased from Abcam. FCCP (HY-100410), CAY10650 (HY-10801), and Arachidonic acid (HY-109590) were purchased from MedChemExpress. NSA was a gift from Dr. Huang Wang (Peking University). TNFα was a gift from Dr. Fuping You (Peking University). Smac was a gift from Dr. Xiaodong Wang (National Institute of Biological Sciences, Beijing). MitoTracker™ Red CMXRos (M7512), Mito Tracker™ Green FM (M7514), TMRM (T668), and Prolong™ Diamond Antifade with DAPI (P36962) were purchased from ThermoFisher Scientific. Other drugs used in this study included EUK134 (TargetMol, T6495), NAC (Shanghai yuanye Bio-Technology, S20137), and H_2O_2 (Aladdin, H112515).

1.4 Cell confinement

Cell confinement was performed using a homemade device consisting of stainless-steel weight, optical glass, and microsphere spacers with different sizes (Bangs Laboratories, USA) (Figure 1A). For biochemical studies, the mixture of cells and microspheres with appropriate volume was planted into the 35 mm culture dish (Corning, 430165) overnight. Then weighted optical glass was carefully and vertically placed on top of the culture substrate. The diameters of the microspheres (20 μm versus 3 μm) determined the height for spatial confinement of cells between the glass and the substrate. Notably, a version of the cell confiner adapted to 35 mm glass-bottom dishes was used to perform high-resolution live cell imaging.

1.5 Microscopy imaging of cell death

Cell death in confinement was evaluated by propidium iodide (PI, Sigma-Aldrich, P4170-10MG) uptake of cells measured by fluorescent microscope. Cells were seeded on the 35 mm culture dish and PI was added to the culture medium at a final concentration of 5 μg/mL before confinement. Static images of dead cells were captured using a 4× dry objective lens on Andor Dragonfly Spinning Disk Confocal Microscopy after confining 8-10 hours. Time-lapse imaging of cell death was recorded with the LIFE EVOS FL Auto fluorescent microscopy (Life Technologies, USA). All images were processed using ImageJ software (https://imagej.nih.gov/ij/). Image data shown were representative of at least three randomly selected fields.

1.6 Measurement of ROS

To detect total ROS, cells were pre-stained with 10 μM DHE (Beyotime, S0063) in culture media at 37℃ for 30 min, and were then washed with PBS twice. To detect lipid ROS, cells were pre-incubated with 5 μM BODIPY-C11 581/591 staining (Abclonal, RM02821) at 37□ for 1 h and washed with PBS twice. After staining, cells were subjected to confinement and fluorescent images were taken by a 10× dry objective lens of CellTIRF microscopy (Olympus, Japan) at different time points. To detect mtROS, cells were stably expressed with Mito-roGFP, and imaging was acquired using a 63× 1.4 NA objective lens on Andor Dragonfly Spinning Disk Confocal Microscopy with the excitation wavelength of 405 nm or 488 nm, and the emission wavelength of 500-550 nm. mtROS level was indicated by the RoGFP ratio, which was calculated as the fluorescence intensity under the excitation wavelength of 405 nm divided by the intensity under the excitation wavelength of 488 nm (405/408 Ratio).

1.7 Western blot

For western blot, cells were washed with PBS and lysed with appropriate volumes of commercial 1× SDS-PAGE sample loading buffer (Beyotime, P0015A) for several minutes. The protein samples were boiled for 15 min at 95□ and were separated on SDS-PAGE gels before being transferred onto NC

membranes by wet electrophoretic transfer. After blocking in PBS containing 5% milk, blots were incubated with the first antibodies at 4℃ overnight or for 2 h at room temperature, followed by the second antibodies incubation for 1 h at room temperature. Blots were visualized and recorded using SH-Compact 523 (SHST). The images were processed by ImageJ software.

1.8 Quantitative real-time PCR

Briefly, total RNA from HeLa cells were isolated using Trizol (Life Technologies, 15596026). RNA was reverse transcribed using a Transcript One-Step gDNA Removal and cDNA Synthesis SuperMix Kit (Transgene, AT311-02). Level of the ASCL4, COX2 and α-tubulin genes were analyzed by qRT-PCR amplified using SYBR Green Fast qPCR Mix (ABclonal, RK21203). Data shown were the relative abundance of the ASCL4 and COX2 mRNA normalized to α-tubulin. The primer sequences used are listed in Table S1.

1.9 Cellular enucleation

Enucleation was performed as previously described [58] with some modifications. Small plastic slides that fit into 1.5 mL Eppendorf tubes were cut from 10 cm cell culture dishes, followed by incubation in 95% ethanol for 10 min and ultraviolet irradiation for 30 min. Before seeding cells, the plastic slides were coated with 10 μg/mL fibronectin solution for 30 min at 37°C. Cells on plastic slides were pre-incubated with DMEM containing 2 μM Cytochalasin D (CytD, Sigma-Aldrich, C2618-200UL) in 1.5 mL Eppendorf tubes for 1 h at 37℃, then the cells were centrifuged at 16,000 g in a GeneSpeed microcentrifuge (Gene Company Limited, 1524) for 30 min. After centrifugation, the remaining cells and cytoplasts on the plastic slides were placed in 10 cm cell culture dishes containing fresh medium without CytD to spread and recover from the effects of CytD fully. About 3 to 4 hours later, the cells were washed with PBS, trypsinized, and reseeded on fibronectin-coated glass-bottom dishes for live cell imaging.

1.10 Atomic force microscopy (AFM) coupled with live cell imaging

To confine a single cell, we used a Bioscope Resolve AFM (Bruker, USA) with the HA_FM tipless silicon probe (force constant, 3 or 6 N/m, ScanSens), and the AFM was mounted on the stage of an inverted fluorescence microscope (ECLIPSE Ti, Nikon) for imaging. Before confinement and imaging, HeLa cells were plated on fibronectin-coated 35 mm glass-bottomed dishes (Cellvis, D35-20-1-N). Experiments were initiated 4-6 h after cell plating to allow for cells to fully spread. During imaging, cells were maintained in CO2-independent DMEM supplemented with 10% FBS, 100 U/mL penicillin, and 100 mg/mL streptomycin. The probe was mounted in the AFM head and the 6 N/m microcantilever was lowered on the cell until a 0.8 V setpoint was reached, at which cells were significantly confined. Meanwhile, fluorescence images were taken every 0.2 seconds using a 100× oil immersion objective to record the whole process of microcantilever lowering. After cells were stably compressed by the cantilever, images were taken every 30 seconds to observe changes in mitochondrial morphology. All microscopy equipment was placed in an acoustic enclosure on the top of the vibration isolation platform.

1.11 Generation of EGFP-Drp1 Knock-in cells

HeLa cell line with an endogenous N-terminal EGFP insertion in the Drp1 gene locus was generated via the CRISPR/Cas9 system. The following sgRNA was generated via the online CRISPR design tool (CRISPOR (tefor.net)) and was cloned into a lentiCRISPR-V2 vector (Addgene, 52961). The donor template contained left homologous arm (840 bp before the start code), EGFP sequence, and right homologous arm (1000 bp after the start code). The homologous arms were amplified from the HeLa cell-extracted genome DNA. Cells were co-transfected with sgRNA and relative donor template plasmid for 24 h and then treated with puromycin (Sigma-Aldrich, P8833) at 2 μg/mL for 24 h. Surviving cells were sorted by Fluorescence Activated Cell Sorting (FACS) to isolate fluorescence-positive cells. The candidate single cell clones were cultured and verified by western blot.

1.12 Protein expression and purification

For recombinant protein expression in *E.coli* BL21-CondonPlus (DE3)-RIPL (AngYu Biotechnologies, AYBIO-G6028), DNA fragments encoding Drp1 were cloned into the modified pET28a (+) vector with an N-terminal His6-tag and a C-terminal EGFP tag as described previously (Liang et al., 2020). Bacteria transformed with plasmid were cultured in LB medium with 50 mg/L kanamycin at 37□ to an OD600 of 0.8-1.0. After that, protein expression was induced with 0.1 mM isopropyl-1-thio-β-D-galactopyranoside (IPTG) for 16 h at 18□.

For protein purification, cell pellets were collected by centrifugation at 4000 g and were suspended in TBS buffer containing 20 mM Tris (pH 8.0), 140 mM NaCl, 30 mM KCl, 10% glycerol, 20 mM imidazole, 0.5 mM TCEP, and protease inhibitor mixture (Complete EDTA-free, Roche). The suspension was lysed by sonication and cleared by centrifugation twice at 4□,13000 g for 30 min. The supernatant was applied to a Ni-IDA column (Smart-Lifesciences) and washed three times using buffers containing 20 mM Tris (pH 8.0), 500 mM NaCl, 0.5 mM TCEP, and different concentrations of imidazole (0 mM, 20 mM, 40 mM). Bound Drp1 proteins were eluted with buffer containing 20 mM Tris (pH8.0), 500 mM NaCl, 0.5 mM TCEP and 300 mM imidazole, and PreScission protease was added to the elution to cleave the N-terminal His_6-tag. Finally, proteins were purified by size exclusion chromatography using Superose 6 Increase 10/300 (GE Healthcare) in buffer containing 20 mM Tris (pH 8.0), 500 mM NaCl and 0.5 mM TCEP. Fractions containing Drp1 were collected, concentrated, and flash frozen in liquid nitrogen. Protein concentrations were measured with NanoDrop 2000 spectrophotometry using the theoretical molar extinction coefficients at 280 nm. Protein purity was evaluated with Coomassie brilliant blue staining of SDS-PAGE gels.

Quality control data of the recombinant Drp-EGFP proteins were shown in Figure S5C-S5D.

1.13 In vitro phase transition assay

Preparing coverslips and glass slides

Glass slides were rinsed with ethanol twice and dried with air. A flow chamber for imaging with two openings on opposite sides was then made by attaching a coverslip (Fisherbrand, 12541016) to the glass slide using double-sided tape placed parallel to each other.

Phase separation assays

Full-length Drp1 and its mutants were labeled by EGFP tags. The purified proteins were saved in a high salt solution containing 500 mM NaCl, 20 mM Tris (pH = 8.0), and 0.5 mM TCEP after protein production. According to different protein and NaCl concentrations for phase separation assay, they were diluted into the corresponding lower salt experimental buffers at a final concentration of 8% dextran to induce phase separation. The protein-phase buffer mixtures were mixed gently. Then, 5 μL mixtures were injected into the homemade flow chamber for fluorescent imaging using the Andor Dragonfly confocal imaging system by putting the chamber upside down on the objective. Notably, the last layer (closest to the lens) of droplets was averted when acquiring the images to minimize the interaction between droplets and the glass surface.

1.14 Generation of knockdown and knockout cells

For Drp1 and cPLA2 knockdown in HeLa cells, the related shRNA were cloned into pLKO.1 vector. After lentivirus infection and puromycin selection, the pooled cells were collected and verified by western blot.

For Drp1 knockout, sgRNA was cloned into the LentiCRISPR-V2 vector, followed by transfection into HeLa cells. After puromycin selection, the single cell clones were cultured and verified by RNA sequence and western blot.

1.15 Measurement of intracellular viscosity

To detect intracellular viscosity upon confinement, HeLa cell stably expressing 40 nm GEM were confined and imaged by a 63× 1.4 NA objective lens on Andor Dragonfly Spinning Disk Confocal Microscopy. Fluorescence images

were taken every 10 ms with 488 nm excitation wavelength and 525 nm emission wavelength at 100% exposure intensity. To analyze the images, tracking of single GEM particle was performed with the Mosaic suite of ImageJ software, using the following typical parameters: radius =3, cutoff=0, 15% of fluorescence intensity, a link range of 1, a maximum displacement of 12 px, and assuming Brownian dynamics.

Following tracking, the time-averaged mean-square displacement (MSD), as well as the ensemble-average of the time-averaged MSD were calculated as previously defined (*Munder et al, 2016*) for curve fitting and obtaining the effective coefficient of diffusion (D_{eff}). There is a linear relationship between MSD and D_{eff} in a short time (*M Delarue et al, 2018*):

$$\mathrm{MSD}_{\mathrm{truncated}}(\tau) = 4D_{\mathrm{eff}}\tau$$

Finally, the distributions of D_{eff} were plotted and the statistical differences were assessed at confinement for 0 min, 10 min, and 60 min using MATLAB and GraphPad Prism 8.0.

1.16 Immunofluorescence staining and imaging analysis

The relative normal and OA cartilage samples from the same patient with OA were frozen in OCT and sectioned into slices attached onto glass slides. Slides were washed by PBS for 5 min and were incubated with PBS containing 10% FBS and 0.3% Triton X-100 for 1 h at room temperature. Then, the slides were incubated with the primary antibodies mix solution containing mouse anti-cPLA2 (1:100), rabbit anti-TOM20 (1:200) and 0.3% Triton X-100 for 2 h at room temperature. After three times of PBS washing for 5 min each, the slides were incubated with anti-mouse Alexa Fluor 488- and anti-rabbit Alexa Fluor 555-conjugated secondary antibodies diluted in 1:200 for 2 h at room temperature. The secondary antibodies mix solution also contained 0.3% Triton X-100. Following another three times washing with PBS, a coverslip was mounted using with ProLong™ Diamond with DAPI. Images were captured by Andor Dragonfly confocal imaging system after mounting medium was

solidified.

To detect total ROS and lipid ROS levels in normal and OA cartilage samples, the slides were washed by PBS for 5 min and stained with DHE probe (50 μM) or BODIPY-C11 581/591 probe (40 μM) for 2 h at 37°C. Following staining, slides were washed three times with PBS for 5 min each and coverslips were mounted using with ProLong™ Diamond with DAPI.

1.17 Statistics and Reproducibility

All data were representative of two or more independent experiments and were mean ± SD as indicated in the figure legends and supplementary figure legends. Statistical significance was determined using two-tailed Student's t-test, one-way or two-way ANOVA analysis with multiple comparisons test. All calculations of significance were performed with GraphPad Prism 8.0.

Reference

1. Labruyère, E. & Guillén, N. Host Tissue Invasion by Entamoeba histolytica Is Powered by Motility and Phagocytosis. *Archives of Medical Research* **37**, 252-257 (2006).

2. Dufour, A.C., Olivo-Marin, J.-C. & Guillen, N. Amoeboid movement in protozoan pathogens. *Seminars in Cell & Developmental Biology* **46**, 128-134 (2015).

3. Balzer, E.M. *et al.* Physical confinement alters tumor cell adhesion and migration phenotypes. *The FASEB Journal* **26**, 4045-4056 (2012).

4. Iskratsch, T., Wolfenson, H. & Sheetz, M.P. Appreciating force and shape — the rise of mechanotransduction in cell biology. *Nature Reviews Molecular Cell Biology* **15**, 825-833 (2014).

5. Uhler, C. & Shivashankar, G.V. Regulation of genome organization and gene expression by nuclear mechanotransduction. *Nature Reviews Molecular Cell Biology* **18**, 717-727 (2017).

6. Liu, Y.J. *et al.* Confinement and low adhesion induce fast amoeboid migration of slow mesenchymal cells. *Cell* **160**, 659-672 (2015).

7. Pagès, D.L. *et al.* Cell clusters adopt a collective amoeboid mode of migration in confined nonadhesive environments. *Sci Adv* **8** (2022).

8. Ekpenyong, A.E. *et al.* Mechanical deformation induces depolarization of neutrophils. *Sci Adv* **3** (2017).

9. Niethammer, P. Components and Mechanisms of Nuclear Mechanotransduction. *Annual Review of Cell and Developmental Biology* **37**, 233-256 (2021).

10. Fletcher, D.A. & Mullins, D. Cell mechanics and the cytoskeleton. *Nature* **463**, 485-492

(2010).

11. Humphrey, J.D., Dufresne, E.R. & Schwartz, M.A. Mechanotransduction and extracellular matrix homeostasis. *Nature Reviews Molecular Cell Biology* **15**, 802-812 (2014).

12. Lomakin, A.J. *et al.* The nucleus acts as a ruler tailoring cell responses to spatial constraints. *Science* **370**, 310-+ (2020).

13. Venturini, V. *et al.* The nucleus measures shape changes for cellular proprioception to control dynamic cell behavior. *Science* **370**, 311-+ (2020).

14. Denais, C.M. *et al.* Nuclear envelope rupture and repair during cancer cell migration. *Science* **352**, 353-358 (2016).

15. Nader, G.P.F. *et al.* Compromised nuclear envelope integrity drives TREX1-dependent DNA damage and tumor cell invasion. *Cell* **184**, 5230-5246 e5222 (2021).

16. Raab, M. ESCRT III repairs nuclear envelope ruptures during cell migration to limit DNA damage and cell death (vol 353, aah6167, 2016). *Science* **353**, 1507-1507 (2016).

17. Nagata, S. & Tanaka, M. Programmed cell death and the immune system. *Nature Reviews Immunology* **17**, 333-340 (2017).

18. Tang, R. *et al.* Ferroptosis, necroptosis, and pyroptosis in anticancer immunity. *Journal of Hematology & Oncology* **13** (2020).

19. Wang, S. *et al.* Mechanical overloading induces GPX4-regulated chondrocyte ferroptosis in osteoarthritis via Piezo1 channel facilitated calcium influx. *Journal of*

Advanced Research **41**, 63-75 (2022).

20. Le Berre, M., Aubertin, J. & Piel, M. Fine control of nuclear confinement identifies a threshold deformation leading to lamina rupture and induction of specific genes. *Integr Biol (Camb)* **4**, 1406-1414 (2012).

21. Logue, J., Logue, J., Chadwick, R. & Waterman, C. A simple method for precisely controlling the confinement of cells in culture. *Protocol Exchange* (2018).

22. Wang, Y.P. *et al.* Chemotherapy drugs induce pyroptosis through caspase-3 cleavage of a gasdermin. *Nature* **547**, 99-+ (2017).

23. Liu, X., Xia, S., Zhang, Z., Wu, H. & Lieberman, J. Channelling inflammation: gasdermins in physiology and disease. *Nature Reviews Drug Discovery* **20**, 384-405 (2021).

24. Shi, J.J. *et al.* Cleavage of GSDMD by inflammatory caspases determines pyroptotic cell death. *Nature* **526**, 660-665 (2015).

25. Zhang, Z. *et al.* Gasdermin E suppresses tumour growth by activating anti-tumour immunity. *Nature* **579**, 415-420 (2020).

26. Chen, S.F. *et al.* RIPK1/RIPK3/MLKL-mediated necroptosis contributes to compression-induced rat nucleus pulposus cells death. *Apoptosis* **22**, 626-638 (2017).

27. Dixon, S.J. *et al.* Ferroptosis: An Iron-Dependent Form of Nonapoptotic Cell Death. *Cell* **149**, 1060-1072 (2012).

28. Jiang, X., Stockwell, B.R. & Conrad, M. Ferroptosis: mechanisms, biology and role in disease. *Nature Reviews Molecular Cell Biology* **22**, 266-282 (2021).

29. Kalukula, Y., Stephens, A.D., Lammerding, J. & Gabriele, S. Mechanics and functional

consequences of nuclear deformations. *Nature Reviews Molecular Cell Biology* **23**, 583-602 (2022).

30. Gaschler, M.M. & Stockwell, B.R. Lipid peroxidation in cell death. *Biochem Bioph Res Co* **482**, 419-425 (2017).

31. Enyedi, B., Jelcic, M. & Niethammer, P. The Cell Nucleus Serves as a Mechanotransducer of Tissue Damage-Induced Inflammation. *Cell* **165**, 1160-1170 (2016).

32. Chao, C.C. *et al.* Metabolic Control of Astrocyte Pathogenic Activity via cPLA2-MAVS. *Cell* **179**, 1483-+ (2019).

33. Efremov, Y.M., Kotova, S.L., Akovantseva, A.A. & Timashev, P.S. Nanomechanical properties of enucleated cells: contribution of the nucleus to the passive cell mechanics. *J Nanobiotechnol* **18** (2020).

34. Graham, D.M. *et al.* Enucleated cells reveal differential roles of the nucleus in cell migration, polarity, and mechanotransduction. *J Cell Biol* **217**, 895-914 (2018).

35. Doll, S. *et al.* ACSL4 dictates ferroptosis sensitivity by shaping cellular lipid composition. *Nature Chemical Biology* **13**, 91-98 (2016).

36. Gao, M.H. *et al.* Role of Mitochondria in Ferroptosis. *Molecular Cell* **73**, 354-+ (2019).

37. Gan, B. Mitochondrial regulation of ferroptosis. *J Cell Biol* **220** (2021).

38. Kraus, F., Roy, K., Pucadyil, T.J. & Ryan, M.T. Function and regulation of the divisome for mitochondrial fission. *Nature* **590**, 57-66 (2021).

39. Smirnova, E., Griparic, L., Shurland, D.L. & van der Bliek, A.M. Dynamin-related protein Drp1 is required for mitochondrial division in mammalian cells. *Molecular*

Biology of the Cell **12**, 2245-2256 (2001).

40. Friedman, J.R. *et al.* ER Tubules Mark Sites of Mitochondrial Division. *Science* **334**, 358-362 (2011).

41. Gregory E. Miner , S.Y.S., Wendy K. Showalter,, Christina M. So, J.V.R., Alex E. Powers, Maria Clara Zanellati , & Chih-Hsuan Hsu, M.F.M., and Sarah Cohen Contact-FP: A Dimerization-Dependent

Fluorescent Protein Toolkit for Visualizing

Membrane Contact Site Dynamics. *Contact* (2024).

42. Weindel, C.G. *et al.* Mitochondrial ROS promotes susceptibility to infection via gasdermin D-mediated necroptosis. *Cell* **185**, 3214-+ (2022).

43. Lei, G., Zhuang, L. & Gan, B.Y. Targeting ferroptosis as a vulnerability in cancer. *Nature Reviews Cancer* **22**, 381-396 (2022).

44. Hill, B. *et al.* The variable domain from the mitochondrial fission mechanoenzyme Drp1 promotes liquid-liquid phase separation. *Biophysical Journal* **121**, 40-40 (2022).

45. Shin, Y. *et al.* Spatiotemporal Control of Intracellular Phase Transitions Using Light-Activated optoDroplets. *Cell* **168**, 159-+ (2017).

46. Bauer, B.L., Rochon, K., Liu, J.C., Ramachandran, R. & Mears, J.A. Disease-associated mutations in Drp1 have fundamentally different effects on the mitochondrial fission machinery. *Hum Mol Genet* **32**, 1975-1987 (2023).

47. Stroka, K.M. *et al.* Water Permeation Drives Tumor Cell Migration in Confined Microenvironments. *Cell* **157**, 611-623 (2014).

48. Delarue, M. *et al.* mTORC1 Controls Phase Separation and the Biophysical Properties

of the Cytoplasm by Tuning Crowding. *Cell* **174**, 338-349.e320 (2018).

49. Eisenhoffer, G.T. *et al.* Crowding induces live cell extrusion to maintain homeostatic cell numbers in epithelia. *Nature* **484**, 546-U183 (2012).

50. Jain, N. & Vogel, V. Spatial confinement downsizes the inflammatory response of macrophages. *Nature Materials* **17**, 1134-1144 (2018).

51. Korobova, F., Ramabhadran, V. & Higgs, H.N. An Actin-Dependent Step in Mitochondrial Fission Mediated by the ER-Associated Formin INF2. *Science* **339**, 464-467 (2013).

52. Wong, Y.C., Ysselstein, D. & Krainc, D. Mitochondria–lysosome contacts regulate mitochondrial fission via RAB7 GTP hydrolysis. *Nature* **554**, 382-386 (2018).

53. Rowland, A.A. & Voeltz, G.K. Endoplasmic reticulum–mitochondria contacts: function of the junction. *Nature Reviews Molecular Cell Biology* **13**, 607-615 (2012).

54. De Magistris, P. & Antonin, W. The Dynamic Nature of the Nuclear Envelope. *Current Biology* **28**, R487-R497 (2018).

55. Alisafaei, F., Jokhun, D.S., Shivashankar, G.V. & Shenoy, V.B. Regulation of nuclear architecture, mechanics, and nucleocytoplasmic shuttling of epigenetic factors by cell geometric constraints. *P Natl Acad Sci USA* **116**, 13200-13209 (2019).

56. Quirós, P.M., Mottis, A. & Auwerx, J. Mitonuclear communication in homeostasis and stress. *Nature Reviews Molecular Cell Biology* **17**, 213-226 (2016).

57. Mohammadi, H. & Sahai, E. Mechanisms and impact of altered tumour mechanics. *Nature Cell Biology* **20**, 766-774 (2018).

58. Efremov, Y.M., Kotova, S.L., Akovantseva, A.A. & Timashev, P.S. Nanomechanical

properties of enucleated cells: contribution of the nucleus to the passive cell mechanics. *J Nanobiotechnology* **18**, 134 (2020).